An Accelerated Model of Modular Isolated DC/DC Converter Used in Offshore DC Wind Farm

Rui Yin, Min Shi, Wenping Hu, Jie Guo, *Member, IEEE*, Pengfei Hu, *Member, IEEE*, and Yifeng Wang

***Abstract*—Modular isolated dc/dc converter (MIDC) is the most important equipment in the offshore dc wind farm. However, the simulation of the accurate MIDC model consumes too much time, which makes it difficult to carry out further studies about this topology. In this paper, an accelerated model that can dramatically decrease the consuming time of the MIDC simulation is proposed. Through an in-depth analysis about the MIDC submodule (SM), the *LLC* series–parallel resonant converter, four equivalent mathematical models that can completely describe the operation modes of the SM are deduced. Thereafter, based on the fourth-order Runge–Kutta method, a detailed design procedure of the MIDC accelerated simulation model is given. Moreover, the influences of different discretization methods on the simulation accuracy and computational speed of the accelerated model are also studied. Finally, the initial simulation model, the nested parent–child simulation method-based simulation model, and the accelerated simulation model of the MIDC with different numbers of SMs are built in the PSCAD/EMTDC. The simulation results prove the effectiveness of the proposed accelerated model.**

***Index Terms*—Accelerated model, fourth-order Runge–Kutta method, mathematical model, modular isolated dc/dc converter (MIDC), offshore dc wind farm.**

I. Introduction

TO MEET the voltage and power requirements of the offshore dc wind farm, the modular isolated dc/dc converter (MIDC) used in the wind farm usually contains large amount of submodules (SMs) [1]–[3]. In these SMs, hundreds of insulated-gate bipolar transistors (IGBTs) and diodes are operated on high frequency to decrease the volume and weight of the isolation transformers [4]–[6]. During the running of an electromagnetic transient simulation software like PSCAD/EMTDC, the inversion of the nodal admittance matrix corresponding to the simulation model is solved first, and then the electric quantities of each node are calculated [7], [8]. Due to the hundreds of switching devices operated on high frequency in the MIDC, the nodal

Manuscript received December 17, 2017; revised April 13, 2018; accepted June 29, 2018. Date of publication July 9, 2018; date of current version February 20, 2019. Recommended for publication by Associate Editor Y.-M. Chen. *(Corresponding author: Rui Yin.)*

R. Yin, M. Shi, and Y. Wang are with State Grid Hebei Electric Power Co., Ltd., Shijiazhuang 050000, China (e-mail:

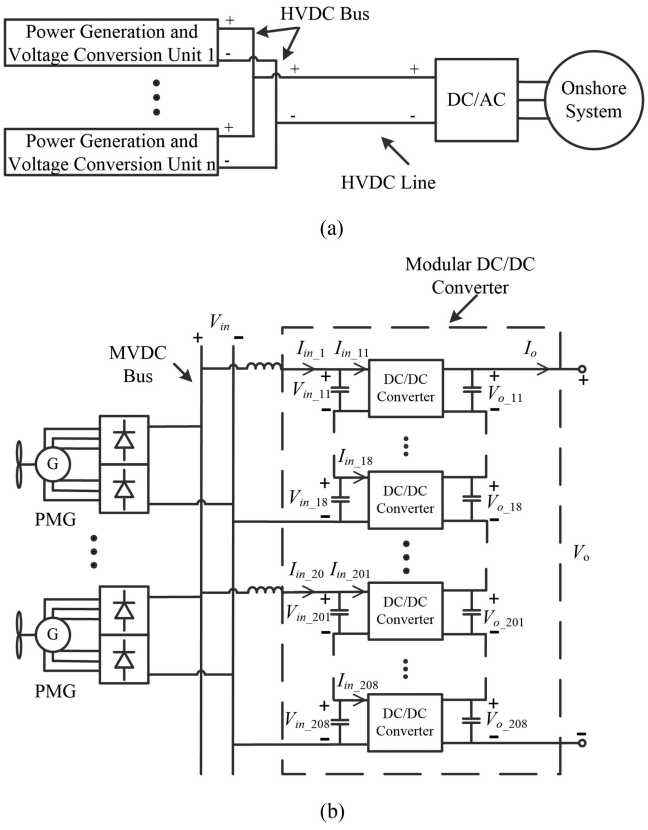

Fig. 1. (a) Configuration of the offshore dc wind farm. (b) Configuration of the MIDC.

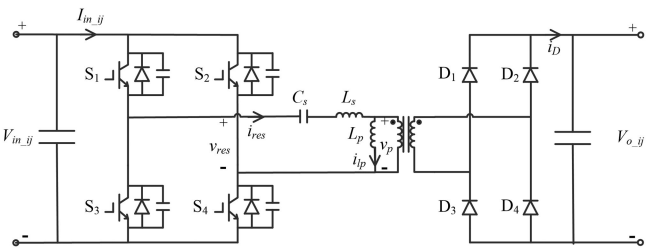

Fig. 2. Schematic circuit diagram of the SM.

II. System Configuration

Fig. 1 shows the configuration of the proposed offshore dc wind farm, which is composed of many power generation and voltage conversion (PGVC) units. Each PGVC unit consists of several adjacent dual three-phase permanent magnet generators (PMGs) and an MIDC. Fig. 1(b) shows the topology of a MIDC with 160 SMs. The 160 SMs are equally divided into 20 SM groups, which are connected in parallel on the input side and series on the output side. Within the SM group, eight SMs are connected in series both on the input and output sides. Based on the series–parallel connection of the SMs, the MIDC can not only meet the high-voltage high-power requirements of the system, but can also realize very high dc voltage gain.

The SM of the MIDC is the *LLC* resonant converter, as shown in Fig. 2. The inverter side of the SM is composed of four IGBT modules and four parallel capacitors while its rectifier side is a full-wave rectifier consisting of four diodes. The resonant tank of the SM is composed of the series resonant capacitor C_s, the series resonant inductor L_s, and the parallel resonant inductor L_m.

III. Accelerated Simulation Model of the MIDC

A. Equivalent Mathematical Model of the SM

To deduce the equivalent mathematical models of the SM, an in-depth analysis about the working conditions of the *LLC* resonant converter is done. In order to simplify the analysis, the following assumptions are made.

1) All the switching devices in the SM are considered as ideal devices.
2) The isolation transformer, inductors, and capacitors in the SM are considered as ideal elements.
3) Ignore the influences of the parallel capacitors of the IGBT modules.
4) Ignore the influences of the dead times.

When used as an SM of the MIDC, the *LLC* resonant converter has two possible working conditions [10], [11], as shown in Fig. 3(a) and (b). In Fig. 3, T_1–T_4 are the trigger signals of S_1– S_4, v_{res} is the input voltage of the resonant tank, i_{res} is the input current of the resonant tank, v_p is the voltage of the parallel resonant inductor, namely, the primary-side voltage of the isolation transformer, i_{lp} is the current through the parallel resonant inductor, and i_D is the output current of the SM.

As shown in Fig. 3(a) and (b), the working conditions 1 and 2 have six and eight stages in one period, respectively. Based on the analysis of the two working conditions, eight operation modes of the SM are plotted in Fig. 4. Within one period, the SM is successively operated on Mode 2 (t_0–t_1), Mode 3 (t_1–t_2), Mode 4 (t_2–t_3), Mode 6, Mode 7, and Mode 8 under working condition 1. Under working condition 2, the SM is successively operated on Mode 1 (t'_0–t'_1), Mode 2 (t'_1–t'_2), Mode 3 (t'_2–t'_3), Mode 4 (t'_3–t'_4), Mode 5, Mode 6, Mode 7, and Mode 8.

Corresponding to the eight operation modes, four equivalent mathematical models of the SM are deduced. Since the operation principle of the SM in the second half period is very similar with the first half period, only the first half period is discussed in this paper. As shown in Fig. 4(a) and (d), the *LLC* resonant converter operated on Modes 1 and 4 can be represented by the same mathematical model, which is

$$v_{res} = V_{in\_ij} \tag{1}$$

$$v_{res} = v_{cs} + v_{ls} + v_p \tag{2}$$

$$i_{res} = C_s \frac{dv_{cs}}{dt} \tag{3}$$

$$v_{ls} = L_s \frac{di_{res}}{dt} \tag{4}$$

$$v_p = L_p \frac{di_{res}}{dt} \tag{5}$$

$$i_p = 0 \tag{6}$$

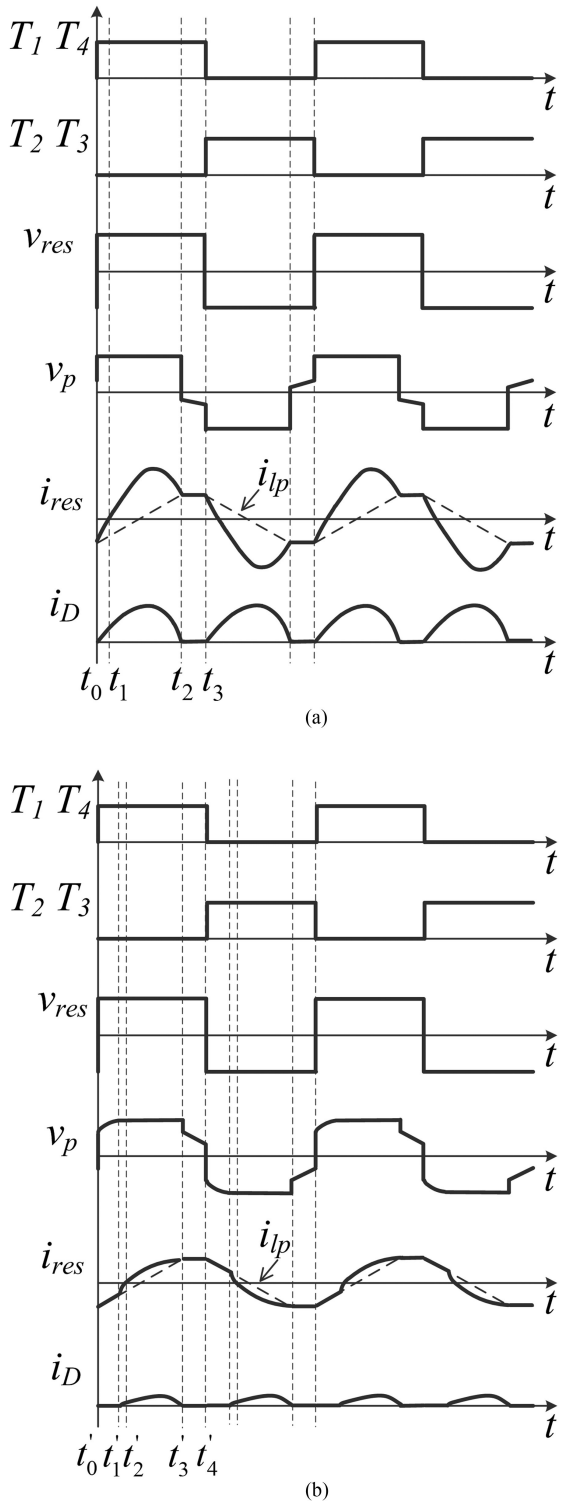

Fig. 3. Two possible working conditions of the *LLC* resonant converter. (a) Working condition 1. (b) Working condition 2.

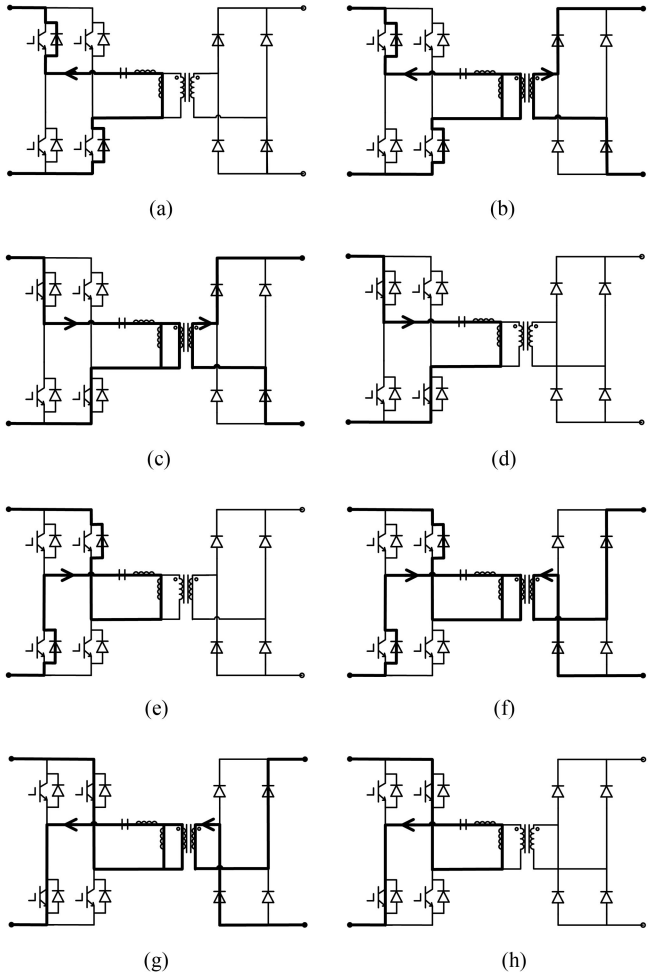

Fig. 4. Eight operation modes of the SM. (a) Mode 1. (b) Mode 2. (c) Mode 3. (d) Mode 4. (e) Mode 5. (f) Mode 6. (g) Mode 7. (h) Mode 8.

where V_{in_ij} is the input voltage of the SM, $i = 1, 2, \ldots, N_{group}$, $j = 1, 2, \ldots, N_{sm}$, N_{group} is the number of the SM groups in one MIDC, N_{sm} is the number of the SMs in one SM group, v_{cs} is the voltage of the series resonant capacitor, v_{ls} is the voltage of the series resonant inductor, and i_p is the primary-side current of the transformer. Define the mathematical model of the SM operated on Modes 1 and 4 as Model 1. The mathematical model of the SM operated on Modes 5 and 8 is defined as Model 3, which can be obtained by substituting V_{in_ij} in (1)–(6) with $-V_{in\_ij}$.

Similarly, as shown in Fig. 4(b) and (c), the *LLC* resonant converter operated on Modes 2 and 3 can be represented by the same mathematical model, which is

$$v_{res} = V_{in\_ij} \tag{7}$$

$$v_{res} = v_{cs} + v_{ls} + v_p \tag{8}$$

$$i_{res} = C_s \frac{dv_{cs}}{dt} \tag{9}$$

$$v_{ls} = L_s \frac{di_{res}}{dt} \tag{10}$$

$$v_p = \frac{V_{o\_ij}}{n_t} = L_p \frac{di_{lp}}{dt} \tag{11}$$

$$i_p = i_{res} - i_{lp} \tag{12}$$

where V_{o_ij} is the output voltage of the SM, and n_t is the transformer ratio. Define the mathematical model of the SM operated

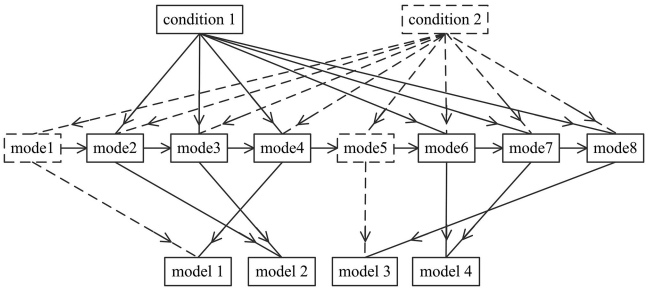

Fig. 5. Relationships of the working conditions, operation modes, and equivalent mathematical models.

on Modes 2 and 3 as Model 2. The mathematical model of the SM operated on Modes 6 and 7 is defined as Model 4, which can be obtained by substituting the V_{in_ij} and V_{o_ij} in (7)–(12) with $-V_{in\_ij}$ and $-V_{o\_ij}$, respectively. The relationships of the SM working conditions, operation modes, and equivalent mathematical models are shown in Fig. 5.

B. Discretization of the Equivalent Mathematical Models

From (1) to (12), it could be known that the equivalent mathematical models of the SM include several ordinary differential equations. To write the corresponding computer program and finally build the MIDC accelerated simulation model, the ordinary differential equations in mathematical models 1 to 4 must be transformed into difference equations. There are many methods that can be used for the discretization. In general, the simpler the discretization method, the simpler the computer program, which means a high computational speed of the simulation model. The disadvantage is a relatively low accuracy. On the contrary, a complicated discretization method means a high accuracy of the simulation model, whereas the computational speed is relatively low. Therefore, there is a tradeoff between the simulation accuracy and the computational speed when the discretization method of the MIDC accelerated model is chosen.

To select a proper discretization method, three SM accelerated simulation models based on the Euler method, the improved Euler method, and the fourth-order Runge–Kutta method, respectively, are built in the PSACD/EMTDC. One conclusion is drawn through a series of simulations of the three SM accelerated models that the complicated discretization method has little influence on the computational speed, but can increase the simulation accuracy obviously. As a result, the fourth-order Runge–Kutta method is finally chosen as the discretization method to build the MIDC accelerated model. The comparisons of three SM accelerated models are presented in Section IV-A. In this section, the discrete result of the SM mathematical models based on the fourth-order Runge–Kutta method is given first.

Take mathematical model 1 as an example, substituting (4) and (5) into (2) yields

$$i'_{res} = \frac{1}{L_s + L_p}\left(V_{in\_ij} - v_{cs}\right). \tag{13}$$

Substituting (3) into (13) yields

$$v''_{cs} = \frac{1}{(L_s + L_p)C_s}(V_{in\_ij} - v_{cs}). \tag{14}$$

Rewriting (3) and (14), the following equations are obtained:

$$\begin{cases} v''_{cs} = \frac{1}{(L_s+L_p)C_s}(V_{in\_ij} - v_{cs}) \\ v'_{cs} = \frac{1}{C_s} i_{res}. \end{cases} \tag{15}$$

Using the fourth-order Runge–Kutta method to discretize (15), we can get

$$\begin{cases} v_{cs}^{n+1} = v_{cs}^{n} + \frac{1}{C_s} i_{res}^{n} \Delta t + \frac{1}{6}(A_1 + A_2 + A_3)\Delta t^2 \\ i_{res}^{n+1} = i_{res}^{n} + \frac{1}{6}(A_1 + 2A_2 + 2A_3 + A_4) C_s \Delta t \end{cases} \tag{16}$$

where

$$\begin{cases} A_1 = \frac{1}{(L_s+L_p)C_s}(V_{in\_ij} - v_{cs}^{n}) \\ A_2 = \frac{1}{(L_s+L_p)C_s}\left(V_{in\_ij} - v_{\mathrm{cs}}^{n} - \frac{1}{2C_s} i_{res}^{n} \Delta t\right) \\ A_3 = \frac{1}{(L_s+L_p)C_s}\left(V_{in\_ij} - v_{cs}^{n} - \frac{1}{2C_s} i_{res}^{n} \Delta t - \frac{1}{4} A_1 \Delta t^2\right) \\ A_4 = \frac{1}{(L_s+L_p)C_s}\left(V_{in\_ij} - v_{cs}^{n} - \frac{1}{C_s} i_{res}^{n} \Delta t - \frac{1}{2} A_1 \Delta t^2\right). \end{cases} \tag{17}$$

According to (2)–(6), and (16), the following equations are obtained:

$$v_p^{n+1} = \frac{L_p}{L_s + L_p}(V_{in\_ij} - v_{cs}^{n+1}) \tag{18}$$

$$i_{lp}^{n+1} = i_{res}^{n+1} \tag{19}$$

$$i_p^{n+1} = 0. \tag{20}$$

Equations (16)–(20) form the discrete model corresponding to mathematical model 1 of the SM. Similarly, the discrete results of mathematical models 2, 3, and 4 can be easily obtained, which are listed in Appendix A.

C. Design of the MIDC Accelerated Model

As mentioned above, the MIDC in the accelerated model is abstracted as a high precision mathematical model directly. Consequently, hundreds of switching devices in the MIDC initial simulation model are omitted and the inversion of a large-scale matrix is avoided. To achieve this target, an SM accelerated model structure shown in Fig. 6 is designed.

As can be seen in Fig. 6, the *LLC* resonant converter in the accelerated model is equivalent to two controlled current sources and two capacitors. Consequently, no more switching devices exist in the circuit topology of the SM. The control signals of two controlled current sources are generated by the computer program module (CPM), as shown in Fig. 6(b). Within the CPM, computer program of the discrete mathematical models 1–4 is written based on the Fortran language. In Fig. 6(b), V_{in_ij}, V_{o_ij}, T_1, and B_{lock} are the input signals of the CPM, I_{in_ij} and i_D are the output signals of the CPM, B_{lock} is the block signal used to block the IGBTs during the fault situations, and I_{in_ij} is the input current of the SM. To simple the MIDC accelerated model, the computer programs of the SMs in one SM group are packaged into one CPM. Therefore, all the input and output signals of

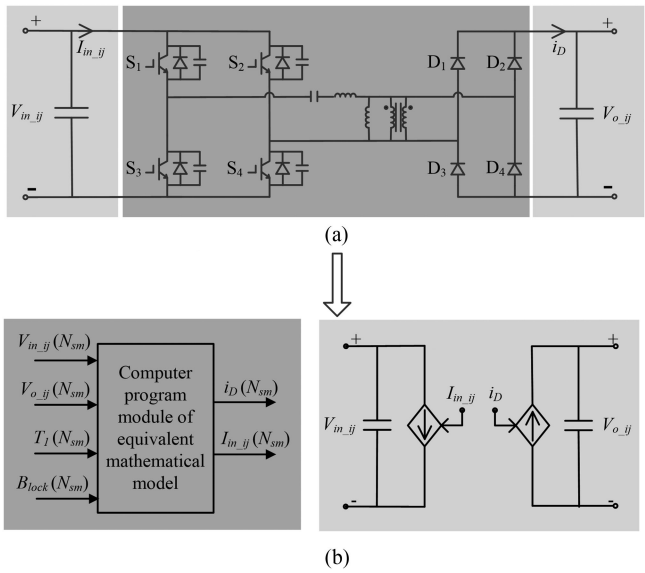

Fig. 6. Structure of the SM accelerated model.

the CPM are N_{sm} dimensional arrays. In an MIDC accelerated model, the number of the CPMs is equal to the number of the SM groups.

According to the analysis in Section III-A, the eight operation modes of the SM can be completely described by the four mathematical models. However, when the computer program is written, not only should the four mathematical models be known, but also the current state of the SM corresponding to which mathematical model should be determined. It should be pointed out that when the operation mode of the SM is changed, the corresponding mathematical model may not change. For example, when the operation mode of the SM under working condition 1 is changed from Modes 2 to 3, the corresponding mathematical model remains unchanged. Therefore, the whole working process of the SM within one period could be redivided according to the mathematical models. Under working condition 1, the equivalent mathematical models of the SM within one period are Model 2 (t_0–t_2), Model 1 (t_2–t_3), Models 4 and 3. Under working condition 2, the equivalent mathematical models of the SM within one period are Model 1 (t'_0–t'_1), Model 2 (t'_1–t'_3), Model 1 (t'_3–t'_4), Model 3, Model 4, and Model 3.

Through the analysis of the two working conditions of the SM, it is known that the changes of the SM equivalent mathematical models could only happen at six different points. In this section, only the three points in the first half period are analyzed as follows.

1) At the rising edge of T_1, namely, at $t = t_0$ of working condition 1 or $t = t'_0$ of working condition 2. At this moment, if the SM is operated under working condition 1, the corresponding mathematical model will change from Models 3 to 2; if the SM is operated under working condition 2, the corresponding mathematical model will change from Models 3 to 1. To decide which working condition the SM is operated, the value of v_p is used. At the rising edge of T_1, if v_p is smaller than V_{o_ij}/n_t, the SM is operated under working condition 2; otherwise, the SM is operated under working condition 1. Therefore, when the computer program of the SM accelerated model is written, whether the rising edge of T_1 appears can be used to decide whether the mathematical model should be changed. After this, the working condition of the SM is decided by the values of v_p and then which mathematical model should be changed to is known.
2) At $t = t'_1$ of working condition 2, namely, at the moment that the value of v_p is increased to V_{o_ij}/n_t from its value at $t = t'_0$. The corresponding mathematical model of the SM is changed from Models 1 to 2 at this moment and the value of v_p is used to identify when this procedure happens.
3) At $t = t_2$ of working condition 1 and $t = t'_3$ of working condition 2, namely, at the moment that the transformer primary-side current i_p is decreased to 0. The corresponding mathematical model of the SM is changed from Models 2 to 1 at this moment and the value of i_p is used to decide when this procedure happens.

Similarly, the changes of the equivalent mathematical models in the second half period are easily obtained, so they will not be covered here.

Based on the aforementioned analysis, the flowchart of the computer program in the CPM is drawn in Fig. 7, where *X* and *Y* are intermediate variables. As shown in Fig. 7, the computer program can detect the rising edge and falling edge of T_1 and then stores the detecting results in *X* and *Y*. The extremely small positive value and negative value in the flowchart are used to help the changes of the mathematical models and have little influence on the accuracy of the accelerated model. Besides, a loop structure is used in the CPM to successively compute all the SMs in one SM group. The output signals of the CPM are obtained through

$$i_D = \left| i_p^{n+1}/n_t \right| \tag{21}$$

$$I_{in\_ij} = k i_{res}^{n+1} \tag{22}$$

where

$$k = \begin{cases} 1 & T_1 = 1 \\ -1 & T_1 = 0. \end{cases}$$

Obviously, the accuracy of the MIDC accelerated model proposed in this paper depends on the accuracy of the equivalent mathematical models of the SM. Compared with the simulation model based on the NPCSM, the accuracy of the accelerated model is relatively lower. However, since the accelerated model simplifies the initial model drastically, its computational speed shows an obvious increase even when compared with the simulation model based on the NPCSM, which will be presented in next section.

IV. Model Validation

A. Influences of Different Discretization Methods on the SM Accelerated Model

In this section, a comparative analysis about three SM accelerated models based on the Euler method, the improved Eu-

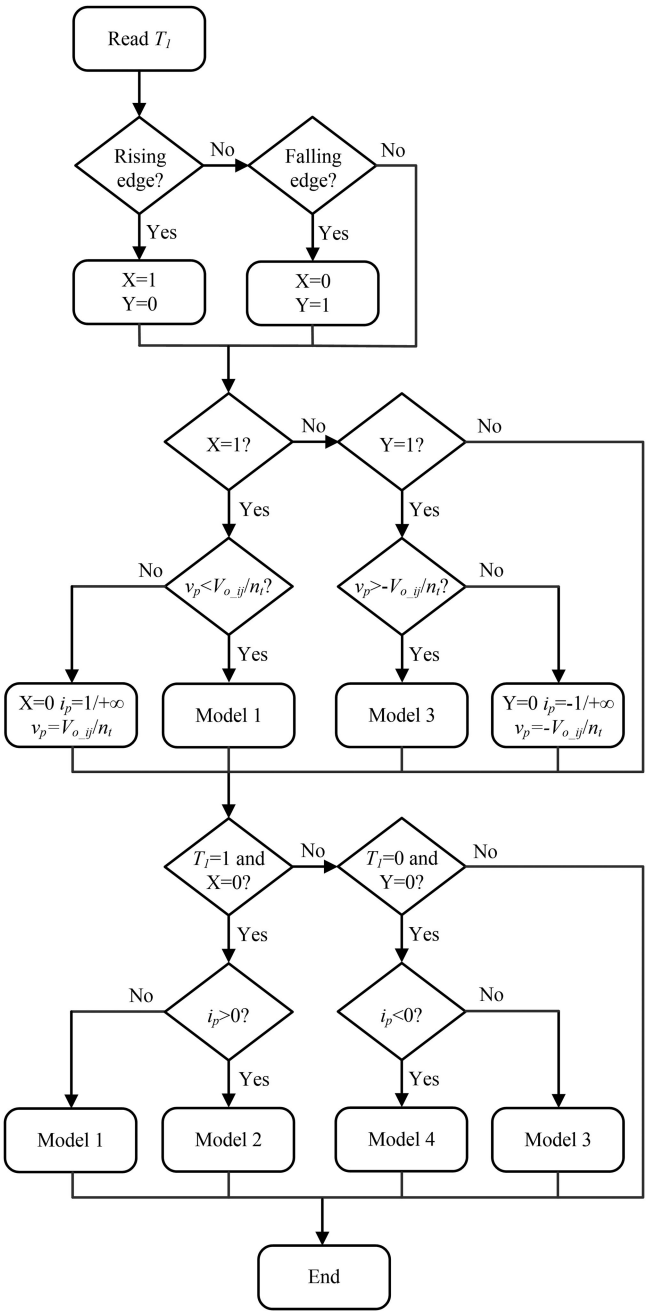

Fig. 7. Program flowchart of the SM accelerated simulation model.

ler method, and the fourth-order Runge–Kutta method, respectively, is done. The schematic circuit diagram of the SM initial simulation model is shown in Fig. 8. In order to keep consistent with the assumptions made in Section III-A, the parallel capacitors of S_1–S_4 shown in Fig. 8 are removed and the dead time is set as a very small value. The schematic circuit diagrams of three SM accelerated models are built according to the topology shown in Fig. 6(b), and the configurations of their input side and output side are similar with that of the initial simulation model. In Fig. 8, R_L is the load resistor, which can be used to regulate the quality factor of the *LLC* resonant converter [12]. The three SM accelerated models and the initial model have exactly

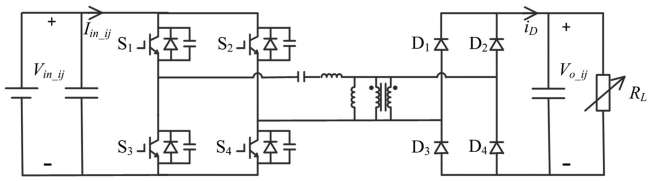

Fig. 8. Schematic circuit diagram of the SM initial simulation mode.

TABLE I
PARAMETERS OF THE FOUR SIMULATION MODELS

Parameter	Value
Rated input voltage	1 kV
Rated output voltage	2.5 kV
Rated input power	0.25 MW
Input side capacitor C_{in}	250 μF
Output side capacitor C_{out}	100 μF
Series resonant capacitor C_s	9.2 μF
Series resonant inductor L_s	76.2 μH
Parallel resonant inductor L_p	381.1μH

the same parameters, as listed in Table I. Moreover, the control systems and control parameters of the four models are exactly the same. The simulation models are running on a Microsoft Windows 7 Operating System with 3.40 GHz Intel Dual-Core i7 CPU, 8 GB of RAM. The version of the PSCAD/EMTDC is 4.2.1.

When the SM input side voltage is set as 1 kV, operation frequency is set as 5 kHz, and R_L is set as 25 Ω, simulation waveforms of the four models with different time steps are shown in Figs. 9 and 10. As shown in Fig. 9, when the time step is set as 0.1 μs, the waveforms of the input and output currents of the three accelerated models are very similar to that of the initial model, which proves the feasibility of the proposed design procedure about the MIDC accelerated model. However, when the time step is set as 0.5 μs, the accuracies of the three SM accelerated models show obvious differences, as shown in Fig. 10. Therefore, it is necessary to make a further comparison about the simulation accuracies and the computational speeds of the three SM accelerated models.

According to the parameters of the MIDC and PMG listed in [10], the operation curve of the *LLC* resonant converter used as the SM of the MIDC can be obtained through a series of simulations. The operation curves of the four simulation models with time steps of 0.1, 0.3, and 0.6 μs are shown in Figs. 11, 12, and 13, respectively. As can be seen in Fig. 11, the operation curves of the four models are very similar when the time step is 0.1 μs. With the increase of the time step, as shown in Figs. 12 and 13, the operation curves of the SM accelerated models based on the Euler method and the improved Euler method present obvious differences with that of the initial model, while the operation curve of the SM accelerated model based on the

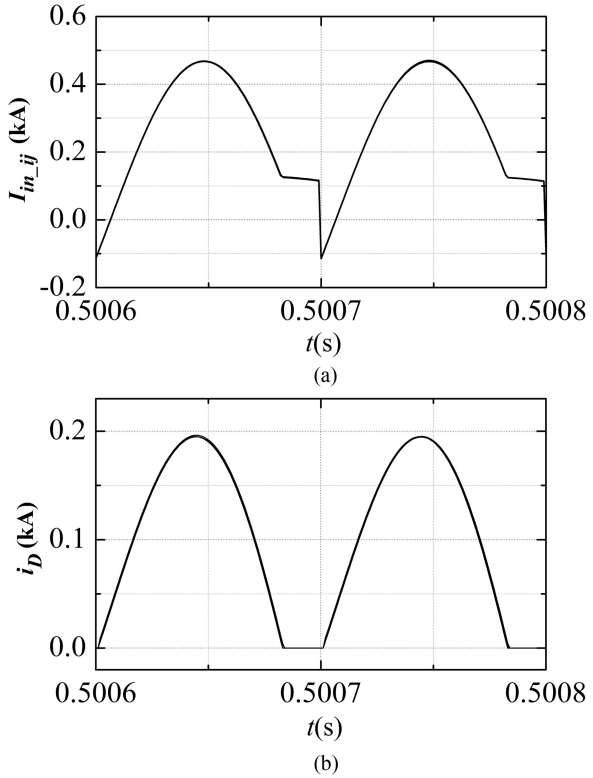

Fig. 9. Simulation waveforms of four SM simulation models with a time step of 0.1 μs. (a) Input currents. (b) Output currents.

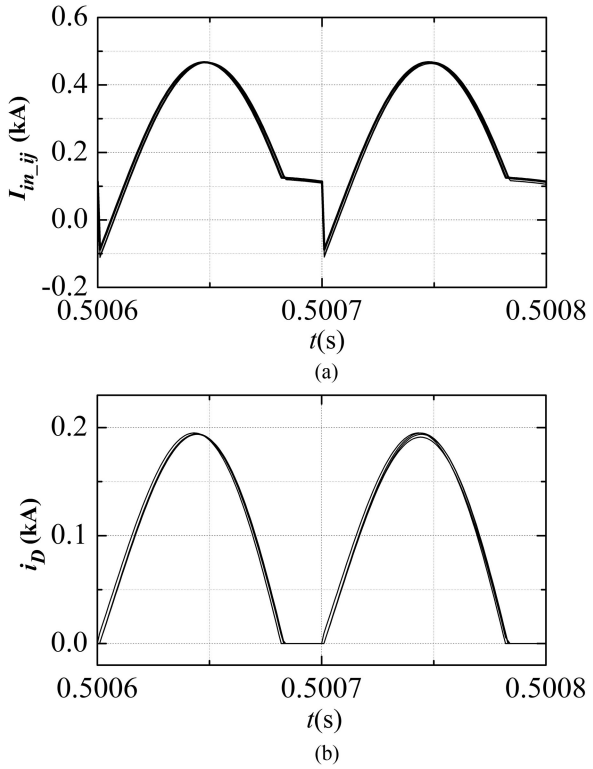

Fig. 10. Simulation waveforms of four SM simulation models with a time step of 0.5 μs. (a) Input currents. (b) Output currents.

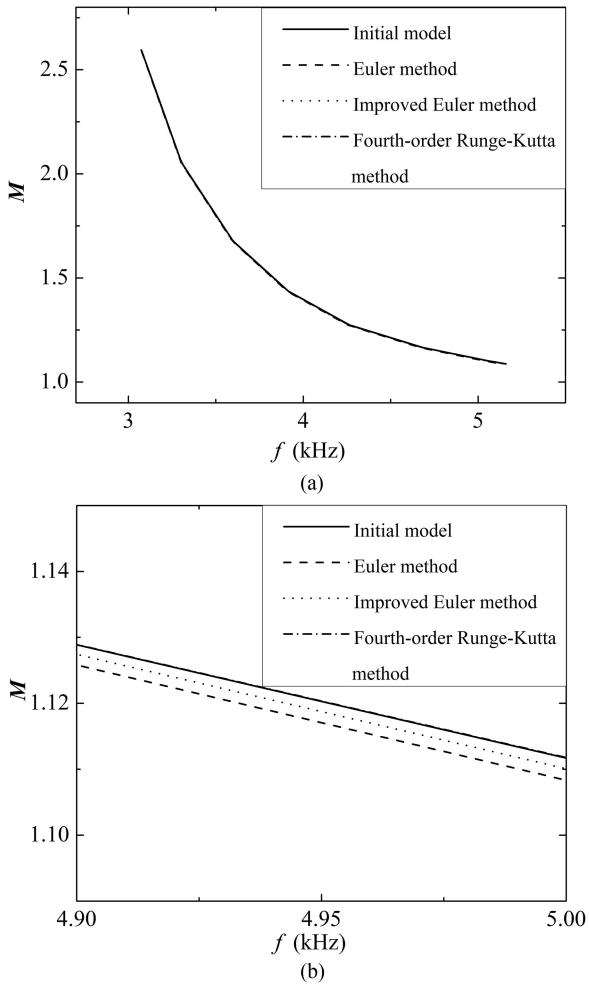

Fig. 11. Operation curves of four SM simulation models with a time step of 0.1 μs. (a) Operation curves of four SM simulation models. (b) An enlarged version of Fig. 11(a).

fourth-order Runge–Kutta method is still almost same as that of the initial model.

When the simulation duration time is set as 1 s, the running times of the four SM simulation models with different time steps are listed in Table II. As can be seen in Table II, the running times of the three SM accelerated models are almost same. The running time of the SM accelerated model based on the fourth-order Runge-Kutta method is just a little bit longer than that of the other two SM accelerated models.

Through the aforementioned analysis, one conclusion is drawn that the SM accelerated model based on the fourth-order Runge–Kutta method has obviously higher accuracy than the other two SM accelerated models, while its drawback of the computational speed is negligible. Consequently, the fourth-order Runge–Kutta method is finally chosen to build the MIDC accelerated model.

B. Transient Performances of the Accelerated Model

In this section, the transient performances of the accelerated model are studied. The topologies of the SM initial model and

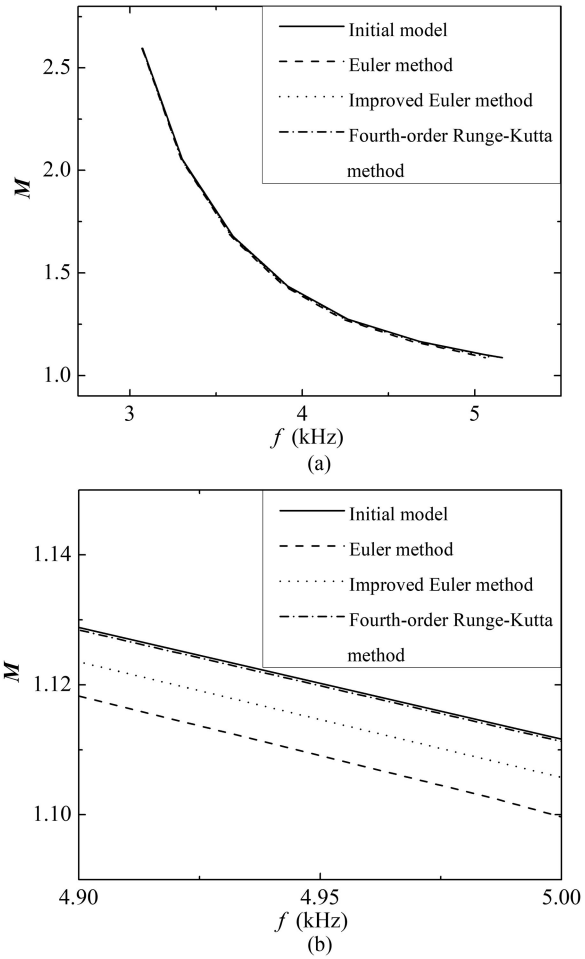

Fig. 12. Operation curves of four SM simulation models with a time step of 0.3 μs. (a) Operation curves of four SM simulation models. (b) An enlarged version Fig. 12(a).

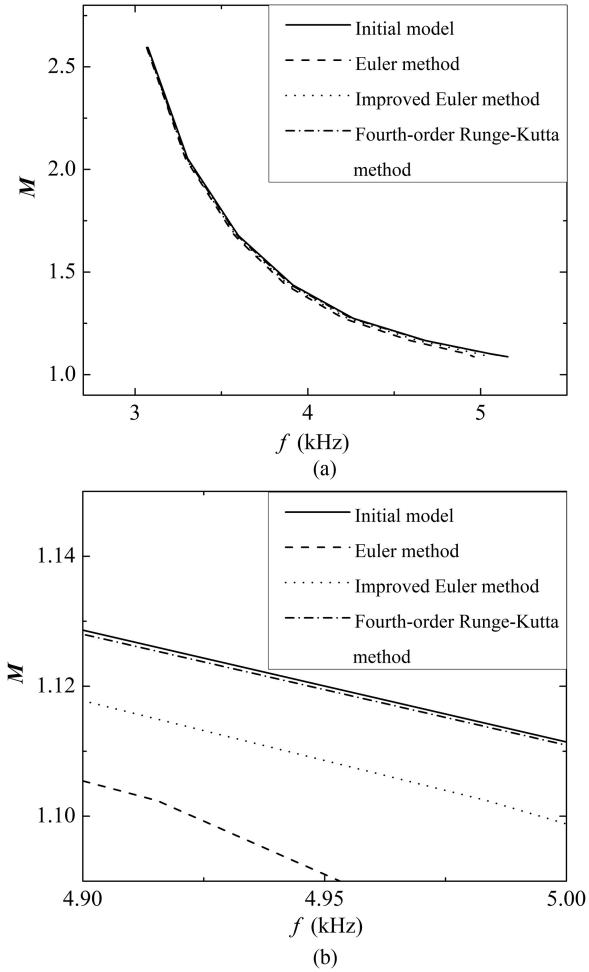

Fig. 13. Operation curves of four SM simulation models with a time step of 0.6 μs. (a) Operation curves of four SM simulation models. (b) An enlarged version Fig. 13(a).

the SM accelerated model are similar to their topologies in Section IV-A. Both the two models are operated on constant output dc voltage control mode. The control systems and control parameters of the two models are exactly the same.

When R_L is set as 50 Ω, the transient performances of the two models with a step change of the input voltage are shown in Fig. 14. In Fig. 14, I_{in_iji} and i_{Di} are the input current and the output current of the SM initial model, respectively, I_{in_ija} and i_{Da} are the input current and the output current of the SM accelerated model, respectively, f_i and f_a are the operation frequencies of the two models, and V_{o_iji} and V_{o_ija} are the output voltages of the two models. At $t = 1$ s, the input voltage of the two models is increased from 0.9 to 1 kV. As can be seen in Fig. 14(a) and (b), when the input voltage is changed, the simulation waveforms of the input and output currents of the two models are almost same. Moreover, the simulation waveforms of the operation frequencies and the output voltages of the two models are also very similar.

Fig. 15 shows the transient performances of the two SM models with a step change of a load resistor. In Fig. 15, I_{Li} and I_{La} are the load currents of the SM initial model and the SM accelerated model, respectively, P_{o_iji} and P_{o_ija} are the output powers of the SM initial model and the SM accelerated model, respectively. At $t = 1$ s, R_L is decreased from 50 to 25 Ω. As shown in Fig. 15(e) and (f), when R_L is decreased to 25 Ω, the load currents of the two models are increased from 0.05 to 0.1 kA and the output powers of the two models are increased from 0.125 to 0.25 MW. During the whole transients, the performances of the two SM models are almost same.

When a short-circuit fault occurs on the output side, the transient performances of the two SM models are shown in Fig. 16. After the fault, the input current of the SM increases

TABLE II
RUNNING TIME OF FOUR SIMULATION MODELS WITH DIFFERENT TIME STEPS

SM simulation model	Time step of 0.1 μs (s)	Time step of 0.3 μs (s)	Time step of 0.6 μs (s)
Initial model	123	43.5	23.5
Euler method based model	20.9	7.9	4.4
Improved Euler method based model	21	7.9	4.5
Fourth-order Runge-Kutta method based model	21.4	8	4.5

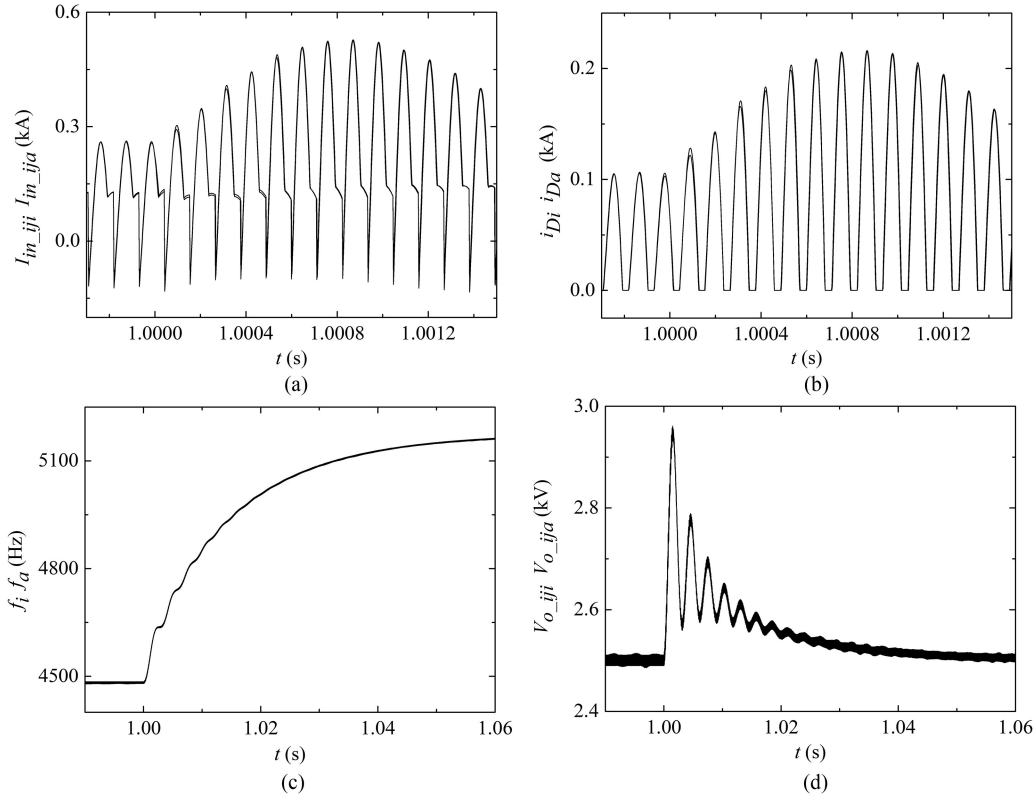

Fig. 14. Transient performances of two SM models with a step change of input voltage. (a) Input currents of two SM models. (b) Output currents of two SM models. (c) Opreration frequencies of two SM models. (d) Output voltage of two SM models.

rapidly. As a result, the overcurrent protection device within the IGBT module will block the IGBT to avoid irreversible damage to the IGBT. When the IGBTs are blocked, the operation modes of the SM are different from the eight modes shown in Fig. 4. A detailed analysis about the operation modes, the corresponding mathematical models, and the accelerated simulation model of the SM during the short-circuit fault is presented in Appendix B.

In Fig. 16, B_{locki} and B_{locka} are the block signals of the SM initial model and the SM accelerated model, respectively, and I_{si} and I_{sa} are the short-circuit currents of the two models. At $t = 1$ s, a short-circuit fault occurs between the two terminals of R_L. R_L is set as 25 Ω and the short-circuit resistor is set as 1 Ω. As shown in Fig. 16(a), the input current of the SM increases quickly after the fault. As a result, the block signals of the two SM models are changed to high level at $t = 1.00012$ s and then all the IGBTs within the two SM models are blocked. Thereafter, the energy stored in the resonant tank of the *LLC* resonant converter is transmitted to the input and output sides of the SM through the antiparallel diodes of the IGBTs and the rectifier diodes of the SM, as shown in Fig. 16(a) and (b). When this process is over, the input and output currents of the SM are decreased to 0. As can be seen in Fig. 16, the transient performances of the SM initial model and the SM accelerated model are very similar under the short-circuit fault condition.

According to the configuration shown in Fig. 1(b), two SM group simulation models are built based on the SM initial model and the SM accelerated model. Within the SM group, eight SMs are connected in series both on the input side and output side. The input side and output side of the SM group are connected to an 8-kV dc voltage source and a 20-kV dc voltage source, respectively. The control strategy presented in [10] is used for the two SM group models and their control parameters are identical. At $t = 1$ s, the input power reference value of the SM group is increased from 1 to 2 MW. The dynamic responses of the two SM group models are shown in Fig. 17. In Fig. 17, I_{in_gi} and I_{in_ga} are the input currents of the two SM group models, I_{o_gi} and I_{o_ga} are the output currents of the two SM group models, and P_{o_gi} and P_{o_ga} are the output powers of the two SM group models. As can be seen, when the input power reference value is changed, the transient performances of the two SM group models are almost same.

C. Validation of the Computational Speed

The initial model, the NPCSM-based model, and the accelerated model of the MIDC with different numbers of SMs are built in the PSCAD/EMTDC. When the simulation duration time is set as 1 s, time step is set as 0.3 μs, the running times of these simulation models are listed in Table III. Since the MIDC initial model is not able to run on an ordinary PC when its SM number reaches 96, the corresponding running times in Table III are not filled in. To present the acceleration effect of the MIDC accelerated model in a straightforward way, the curves of the running times listed in Table III are drawn in Fig. 18. As shown in Fig. 18, compared with the MIDC initial model, both

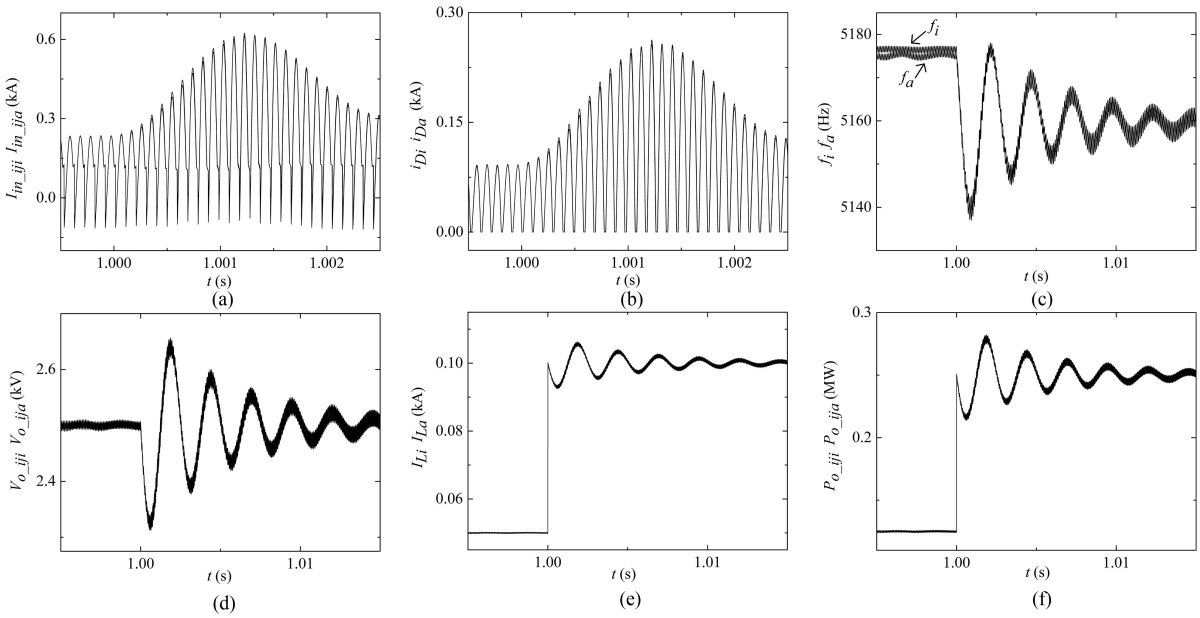

Fig. 15. Transient performances of two SM models with a step change of a load resistor. (a) Input currents of two SM models. (b) Output currents of two SM models. (c) Operation frequencies of two SM models. (d) Output voltage of two SM models. (e) Load currents of two SM models. (f) Output powers of two SM models.

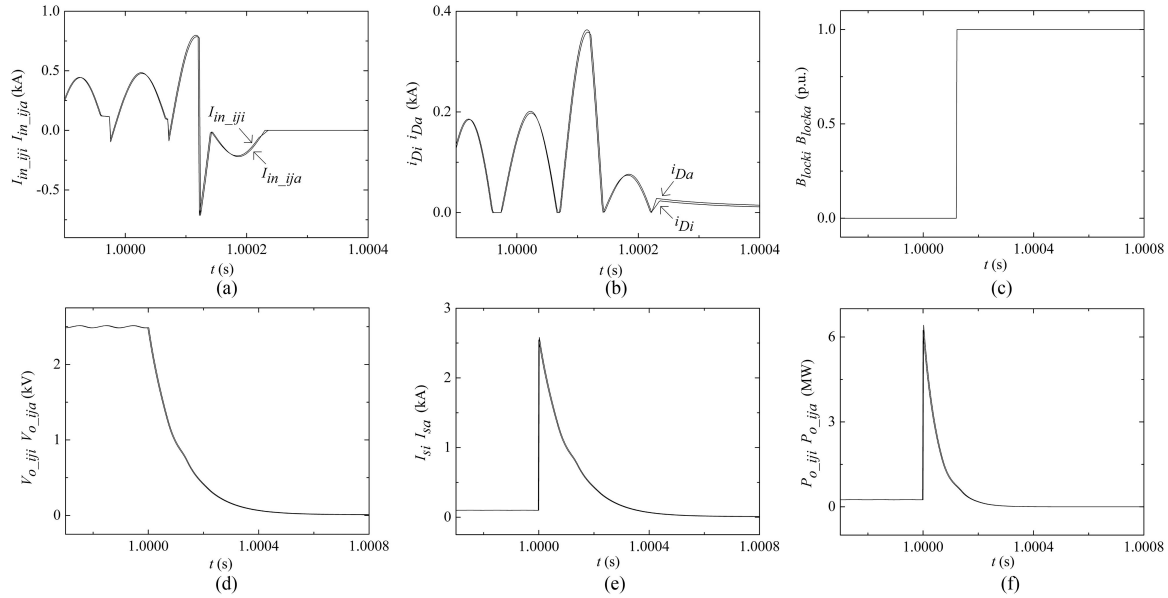

Fig. 16. Transient performances of two SM models with a short-circuit fault on their output sides. (a) Input currents of two SM models. (b) Output currents of two SM models. (c) Block signals of two SM models. (d) Output voltage of two SM models. (e) Short-circuit currents of two SM models. (f) Output powers of two SM models.

the NPCSM-based model and the accelerated model can significantly increase the computational speed. For example, when the number of SMs is 40, the acceleration ratios of the NPCSM-based model and the accelerated model are 218.37 and 1413.9, respectively.

What is more, as shown in Table III and Fig. 18, the MIDC accelerated model has a five to seven times increase on the computational speed even when compared with the NPCSM-based MIDC model. This phenomenon can be explained by the working principle of the PSCAD/EMTDC. Both the accelerated model and the NPCSM-based model can avoid inversing the large-scale nodal admittance matrix. However, in the accelerated model, large amounts of switching devices and passive devices are abstracted as equivalent mathematical models, which replace the detailed and complex component models in the PSCAD/EMTDC. As a result, the computational speed of the MIDC accelerated model is further increased than that of the NPCSM-based model.

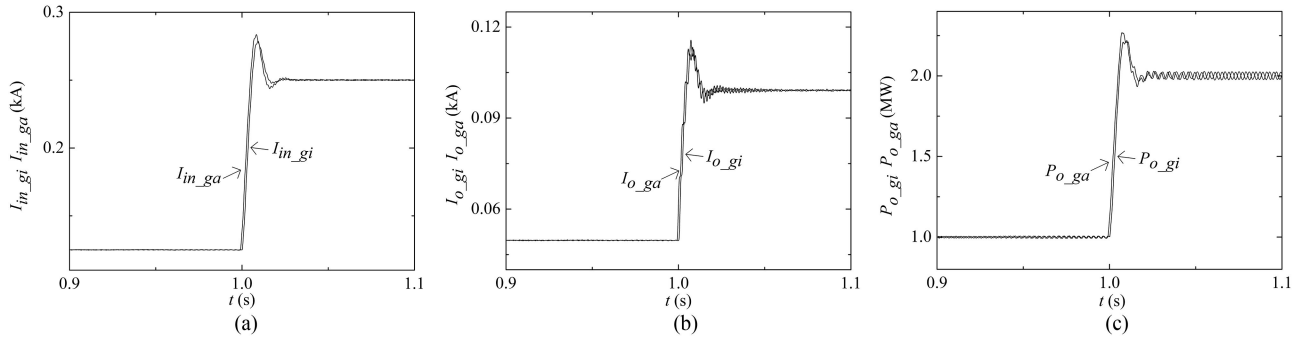

Fig. 17. Transient performances of the two SM group models. (a) Input currents of two SM models. (b) Output currents of two SM models. (c) Operation frequencies of two SM models.

TABLE III
RUNNING TIMES OF DIFFERENT MIDC SIMULATION MODELS

SM number	Running time (s)			Acceleration ratio than initial model		Acceleration ratio of accelerated model than NPCSM model
	Initial model	NPCSM model	Accelerated model	NPCSM model	Accelerated mode	
1	43.5	43.5	8	1	5.44	5.44
8	505	266	37	1.90	13.65	7.19
16	2,789	548	73	5.09	38.21	7.51
40	306,816	1405	217	218.37	1413.90	6.47
96	——	3448	633	——	——	5.45
160	——	6529	1250	——	——	5.22

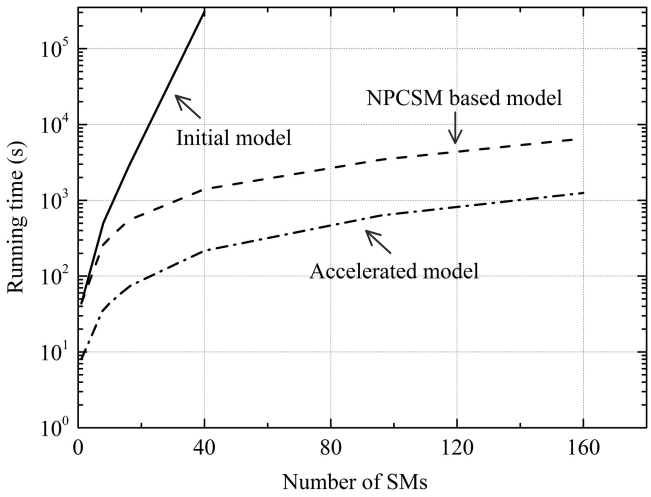

Fig. 18. Running times of different MIDC simulation models.

V. CONCLUSION

In this paper, an accelerated simulation model of the MIDC is proposed and validated. According to the simulation results, the accelerated model can dramatically increase the computational speed compared with the MIDC initial simulation model. Even when compared with the NPCSM-based model, the accelerated model has a five to seven times increase on the computational speed. Meanwhile, through an elaborate design, the simulation accuracy of the accelerated model can be maintained on a relatively high level.

The influences of different discretization methods on the accelerated model are studied, which prove that the more complicated discretization method has little influence on the computational speed, but can obviously increase the simulation accuracy. As a result, the fourth-order Runge–Kutta method is finally chosen to build the MIDC accelerated model.

The design procedure proposed in this paper is also useful for the simulation model building of any other modular dc/dc converter topologies based on the *LLC* resonant converter.

APPENDIX A

The discrete results of mathematical model 2 are

$$\begin{cases} v_{cs}^{n+1} = v_{cs}^{n} + \frac{1}{C_s} i_{res}^{n} \Delta t + \frac{1}{6}(B_1 + B_2 + B_3)\Delta t^2 \\ i_{res}^{n+1} = i_{res}^{n} + \frac{1}{6}(B_1 + 2B_2 + 2B_3 + B_4) C_s \Delta t \end{cases} \tag{23}$$

$$\begin{cases} B_1 = \frac{1}{L_s C_s}\left(V_{in\_ij} - \frac{V_{o\_ij}}{n_t} - v_{cs}^{n}\right) \\ B_2 = \frac{1}{L_s C_s}\left(V_{in\_ij} - \frac{V_{o\_ij}}{n_t} - v_{cs}^{n} - \frac{1}{2C_s} i_{res}^{n} \Delta t\right) \\ B_3 = \frac{1}{L_s C_s}\left(V_{in\_ij} - \frac{V_{o\_ij}}{n_t} - v_{cs}^{n} - \frac{1}{2C_s} i_{res}^{n} \Delta t - \frac{1}{4} B_1 \Delta t^2\right) \\ B_4 = \frac{1}{L_s C_s}\left(V_{in\_ij} - \frac{V_{o\_ij}}{n_t} - v_{cs}^{n} - \frac{1}{C_s} i_{res}^{n} \Delta t - \frac{1}{2} B_1 \Delta t^2\right) \end{cases} \tag{24}$$

$$v_p^{n+1} = \frac{V_{o\_ij}}{n_t} \tag{25}$$

$$i_{lp}^{n+1} = i_{lp}^{n} + \frac{V_{o\_ij}}{n_t L_p}\Delta t \tag{26}$$

$$i_p^{n+1} = i_{res}^{n+1} - i_{lp}^{n+1}. \tag{27}$$

The discrete results of mathematical model 3 are

$$\begin{cases} v_{cs}^{n+1} = v_{cs}^{n} + \frac{1}{C_s} i_{res}^{n}\Delta t + \frac{1}{6}(C_1 + C_2 + C_3)\Delta t^2 \\ i_{res}^{n+1} = i_{res}^{n} + \frac{1}{6}(C_1 + 2C_2 + 2C_3 + C_4)C_s\Delta t \end{cases} \tag{28}$$

$$\begin{cases} C_1 = \frac{1}{(L_s+L_p)C_s}(-V_{in\_ij} - v_{cs}^{n}) \\ C_2 = \frac{1}{(L_s+L_p)C_s}\left(-V_{in\_ij} - v_{cs}^{n} - \frac{1}{2C_s} i_{res}^{n}\Delta t\right) \\ C_3 = \frac{1}{(L_s+L_p)C_s}\left(-V_{in\_ij} - v_{cs}^{n} - \frac{1}{2C_s} i_{res}^{n}\Delta t - \frac{1}{4}C_1\Delta t^2\right) \\ C_4 = \frac{1}{(L_s+L_p)C_s}\left(-V_{in\_ij} - v_{cs}^{n} - \frac{1}{C_s} i_{res}^{n}\Delta t - \frac{1}{2}C_1\Delta t^2\right) \end{cases} \tag{29}$$

$$v_p^{n+1} = \frac{L_p}{L_s + L_p}\left(-V_{in\_ij} - v_{cs}^{n+1}\right) \tag{30}$$

$$i_{lp}^{n+1} = i_{res}^{n+1} \tag{31}$$

$$i_p^{n+1} = 0. \tag{32}$$

The discrete results of mathematical model 4 are

$$\begin{cases} v_{cs}^{n+1} = v_{cs}^{n} + \frac{1}{C_s} i_{res}^{n}\Delta t + \frac{1}{6}(D_1 + D_2 + D_3)\Delta t^2 \\ i_{res}^{n+1} = i_{res}^{n} + \frac{1}{6}(D_1 + 2D_2 + 2D_3 + D_4)C_s\Delta t \end{cases} \tag{33}$$

$$\begin{cases} D_1 = \frac{1}{L_s C_s}\left(-V_{in\_ij} + \frac{V_{o\_ij}}{n_t} - v_{cs}^{n}\right) \\ D_2 = \frac{1}{L_s C_s}\left(-V_{in\_ij} + \frac{V_{o\_ij}}{n_t} - v_{cs}^{n} - \frac{1}{2C_s} i_{res}^{n}\Delta t\right) \\ D_3 = \frac{1}{L_s C_s}\left(-V_{in\_ij} + \frac{V_{o\_ij}}{n_t} - v_{cs}^{n} - \frac{1}{2C_s} i_{res}^{n}\Delta t - \frac{1}{4}D_1\Delta t^2\right) \\ D_4 = \frac{1}{L_s C_s}\left(-V_{in\_ij} + \frac{V_{o\_ij}}{n_t} - v_{cs}^{n} - \frac{1}{C_s} i_{res}^{n}\Delta t - \frac{1}{2}D_1\Delta t^2\right) \end{cases} \tag{34}$$

$$v_p^{n+1} = -\frac{V_{o\_ij}}{n_t} \tag{35}$$

$$i_{lp}^{n+1} = i_{lp}^{n} - \frac{V_{o\_ij}}{n_t L_p}\Delta t \tag{36}$$

$$i_p^{n+1} = i_{res}^{n+1} - i_{lp}^{n+1}. \tag{37}$$

APPENDIX B

When a short-circuit fault occurs at the output side of the SM, the amplitude of i_{res} increases very quickly. After the IGBTs within the SM are blocked at a relatively high value of i_{res}, the operation of the SM can be divided into two stages. In the first stage, the possible operation modes of the *LLC* resonant converter are shown in Fig. 19(a) and (b). If $i_{res} > 0$, the SM will operate on Mode 9; otherwise, the SM will operate on Mode 10. At every time of i_{res} passes through zero, if $|v_{cs}| > V_{in\_ij}$, the SM will continually operate in the first stage. Otherwise, the SM will enter the second stage and the possible operation modes of the SM are shown in Fig. 19(c) and (d). If $i_{lp} < 0$, the SM will operate on Mode 11; otherwise, the SM will operate on Mode 12. In the second stage, $|i_{lp}|$ is decreased to 0 gradually by the output side voltage of SM. When $|i_{lp}|$ reaches 0, the second stage is over.

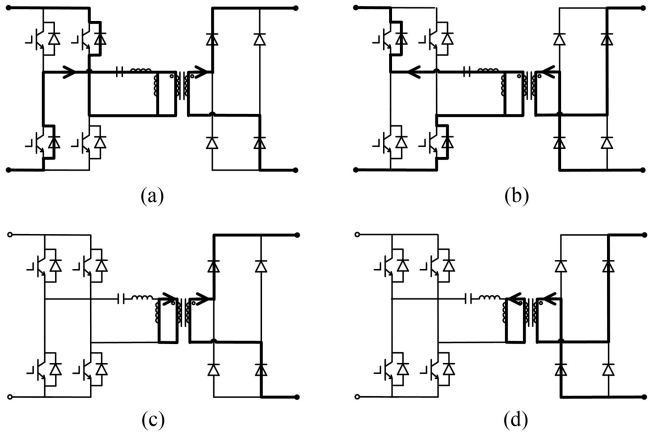

Fig. 19. Possible operation modes of the *LLC* resonant converter after the IGBTs are blocked. (a) Mode 9. (b) Mode 10. (c) Mode 11. (d) Mode 12

The equivalent mathematical model of the SM operated on Mode 9 is defined as Model 5, which can be obtained by substituting V_{in_ij} in mathematical model 2 with $-V_{in\_ij}$. Similarly, the discrete results of Model 5 can be obtained by substituting V_{in_ij} in the discrete results of Model 2 with $-V_{in\_ij}$. The equivalent mathematical model of the SM operated on Mode 10 can be obtained by substituting V_{o_ij} in mathematical model 2 with $-V_{o\_ij}$ and this mathematical model is defined as Model 6. The discrete results of Model 6 can be obtained by substituting V_{o_ij} in the discrete results of Model 2 with $-V_{o\_ij}$.

The equivalent mathematical model of the SM operated on Mode 11 is

$$v_p = \frac{V_{o\_ij}}{n_t} = L_p\frac{di_{lp}}{dt} \tag{38}$$

$$i_p = -i_{lp}. \tag{39}$$

Define (38) and (39) as mathematical model 7. The discrete results of Model 7 are

$$i_{lp}^{n+1} = i_{lp}^{n} + \frac{V_{o\_ij}}{n_t L_p}\Delta t \tag{40}$$

$$i_p^{n+1} = -i_{lp}^{n+1}. \tag{41}$$

The equivalent mathematical model of the SM operated on Mode 12 is

$$v_p = -\frac{V_{o\_ij}}{n_t} = L_p\frac{di_{lp}}{dt} \tag{42}$$

$$i_p = -i_{lp}. \tag{43}$$

Define (42) and (43) as mathematical model 8. The discrete results of Model 8 are

$$i_{lp}^{n+1} = i_{lp}^{n} - \frac{V_{o\_ij}}{n_t L_p}\Delta t \tag{44}$$

$$i_p^{n+1} = -i_{lp}^{n+1}. \tag{45}$$

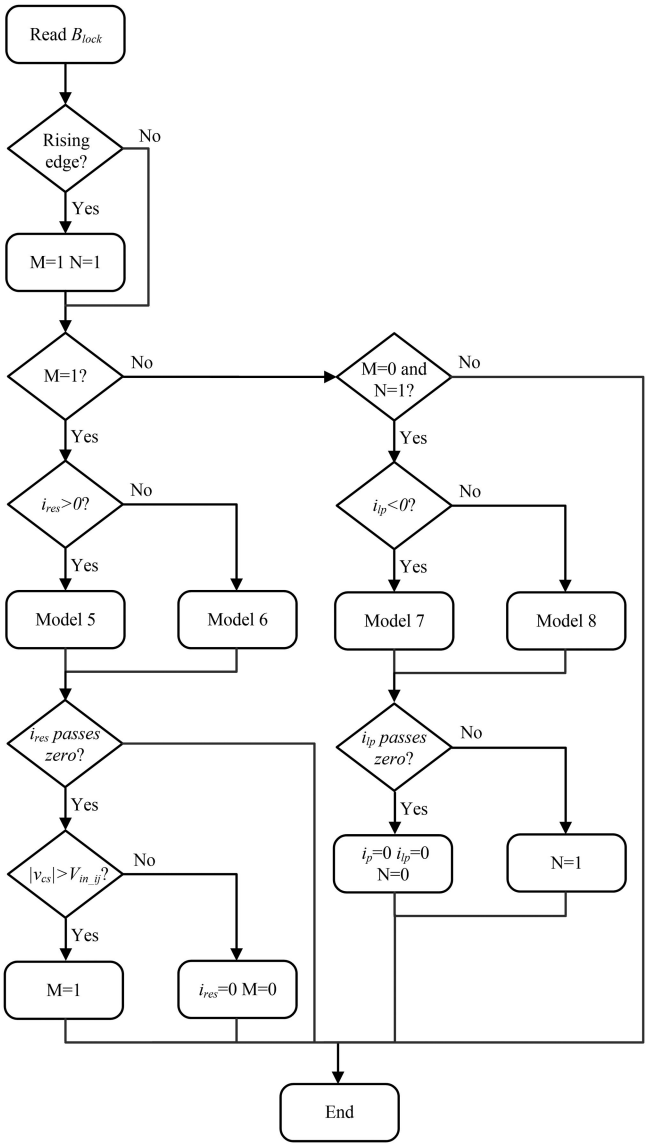

Fig. 20. Program flowchart of the SM accelerated model during the fault situations.

The program flowchart of the SM accelerated model during the fault conditions is shown in Fig. 20. In Fig. 20, *M* and *N* are intermediate variables. After the IGBTs are blocked, the output signals of the CPM can be obtained through

$$i_D = \left| i_p^{n+1}/n_t \right| \tag{46}$$

$$I_{in\_ij} = -|i_{res}^{n+1}|. \tag{47}$$

REFERENCES

[1] K. Sano and M. Takasaki, "A boost conversion system consisting of multiple DC-DC converter modules for interfacing wind farms and HVDC transmission," in *Proc. IEEE Energy Convers. Congr. Expo*., 2013, pp. 2613–2618.

[2] N. Denniston, A. Massoud, S. Ahmed, and P. Enjeti, "Multiple-module high-gain high-voltage DC–DC transformers for offshore wind energy systems," *IEEE Trans. Ind. Electron.*, vol. 58, no. 5, pp. 1877–1886, May 2011.

[3] A. A. Aboushady, K. H. Ahmed, and B. W. Williams, "Compact multi-modular design of high power DC/DC resonant converters for offshore wind energy HVDC transmission," in *Proc. 39th Annu. Conf. IEEE Ind. Electron. Soc.*, 2013, pp. 5236–5241.

[4] A. J. B. Bottion, and I. Barbi, "Input-series and output-series connected modular output capacitor full-bridge PWM DC–DC converter," *IEEE Trans. Ind. Electron.*, vol. 62, no. 10, pp. 6213–6221, Oct. 2015.

[5] W. Chen, X. Ruan, H. Yan, and C. Tse, "DC/DC conversion systems consisting of multiple converter modules: Stability, control, and experimental verifications," *IEEE Trans. Power Electron.*, vol. 24, no. 6, pp. 1463–1474, Jun. 2009.

[6] S. P. Engel, M. Stieneker, N. Soltau, S. Rabiee, H. Stagge, and R. De Doncker, "Comparison of the modular multilevel DC converter and the dual-active bridge converter for power conversion in HVDC and MVDC grids," *IEEE Trans. Power Electron.*, vol. 30, no. 1, pp. 124–137, Jan. 2015.

[7] *PSCAD X4 User's Guide*, Manitoba Research Center, Winnipeg, MB, Canada, 2009.

[8] J. Xu, C. Zhao, W. Liu, and C. Guo, "Accelerated model of modular multilevel converters in PSCAD/EMTDC," *IEEE Trans. Power Del.*, vol. 28, no. 1, pp. 129–136, Jan. 2013.

[9] K. Strunz and E. Carlson, "Nested fast and simultaneous solution for time-domain simulation of integrative power-electric and electronic systems," *IEEE Trans. Power Del.*, vol. 22, no. 1, pp. 277–287, Jan. 2007.

[10] R. Yin, J. Daozhuo, T. Weijia, Z. Yang, L. Yiqiao, D. Yi, "Modular isolated DC/DC converter based grid-connection scheme for offshore DC wind farm," *Automat. Elect. Power Syst.*, vol. 40, no. 17, pp. 190–196, Sep. 10, 2016.

[11] J. F. Lazar and R. Martinelli, "Steady-state analysis of the LLC series resonant converter," in *Proc. 16th Annu. IEEE Appl. Power Electron. Conf. Expo.*, vol. 2, 2001, pp. 728–735.

[12] *Half-Bridge LLC Resonant Converter Design Using FSFR-Series Fairchild Power Switch (FPS™)*, Application Note AN-4151, Fairchild Semicond. Corporation, South Portland, Maine, USA, 2007.

Rui Yin was born in Hengshui, China, on June 12, 1990. He received the B.E. degree in power system and its automation from North China Electric Power University, Baoding, China, in 2012, and the Ph.D. degree in electrical engineering from Zhejiang University, Hangzhou, China, in 2017.

He is currently an Engineer with State Grid Hebei Electric Power Co., Ltd., Shijiazhuang, China. His current research interests include renewable energy generation systems, HVdc and smart grids.

Min Shi received the B.E. degree in electrical engineering from the Xian Jiaotong University, Xian, China, in 1999.

He is currently a Senior Engineer with State Grid Hebei Electric Power Co., Ltd., Shijiazhuang, China. His current research interests include power system operation and control, renewable energy generation systems.

Wenping Hu was born in Xingtai, China, on October 16, 1968. He received the Ph.D. degree in electrical engineering from the Huazhong University of Science and Technology, Wuhan, China, in 2005.

He is currently a Professor with State Grid Hebei Electric Power Research Institute, Shijiazhuang, China. His current research interests include power system operation and control, renewable energy generation systems and power quality.

Jie Guo (S'10–M'13) received the B.E. degree in power system and its automation from North China Electric Power University, Baoding, China, in 2008, and the Ph.D. degree in electrical engineering from Zhejiang University, Hangzhou, China, in 2013.

He is currently a Senior Engineer with State Grid Hebei Electric Power Research Institute, Shijiazhuang, China. His current research interests include renewable energy generation systems, smart grids, and power electronics.

Pengfei Hu (S'13–M'17) received the B.E. and Ph.D. degrees in electrical engineering from Zhejiang University, Hangzhou, China, in 2010 and 2015, respectively.

From 2015 to 2016, he was a Power Engineer with State Grid Sichuan Electric Power Research Institute, Chengdu, China. Since 2017, he has been an Assistant Professor with the University of Electronic Science and Technology of China, Chengdu. He is currently a Visiting Professor with the Department of Energy Technology, Aalborg University, Aalborg, Denmark, as part of the Denmark Micro-grids Group and Modular Mulitlevel Converter Group. His research interests include modular multilevel converters, HVdc, microgrids, and renewable energy generation systems.

Yifeng Wang was born in Nantong, China, on November 11, 1982. He received the B.E. degree in power system and its automation from Southeast University, Nanjing, China, in 2005, and the master's degree in electrical engineering from North China Electric Power University, Baoding, China, in 2017.

He is currently a Senior Engineer with State Grid Hebei Electric Power Co., Ltd., Shijiazhuang, China. His current research interests include power system operation and control, renewable energy generation systems.